JCTC Journal of Chemical Theory and Computation

pubs.acs.org/JCTC Article

Determination of van der Waals Parameters Using a Double Exponential Potential for Nonbonded Divalent Metal Cations in TIP3P Solvent

Viet Hoang Man, Xiongwu Wu,* Xibing He, Xiang-Qun Xie, Bernard R. Brooks,* and Junmei Wang*

Cite This: J. Chem. Theory Comput. 2021, 17, 1086−1097 Read Online

ACCESS | Metrics & More | Article Recommendations | Supporting Information

ABSTRACT: A double exponential (DE) functional form for Lennard-Jones (LJ) interactions, proposed in our previous study, has many advantages over LJ potentials including a natural softcore characteristic for the convenience of the pathway-based free-energy calculations, fast convergence, and flexibility in use. In this work, we put the first step on the application of the DE functional form by identifying a DE potential, coined DE-TIP3P, for molecular simulations using the TIP3P water model. The developed DE-TIP3 potential was better than LJ potential in reproducing the experimental water properties. Afterward, we developed the nonbonded models of 15 divalent metal ions, which frequently appear and play vital roles in biological systems, to be consistent with the DE-TIP3P potential and TIP3P water model. Our nonbonded models were as good as the complicated nonbonded dummy cationic models by Jiang et al. and the nonbonded 12-6-4 LJ models by Li and Merz in reproducing the experimental properties of those ions. Moreover, our nonbonded models achieved a better performance than the compromise (CM) LJ models and 12-6-4 LJ models, developed by Li and Merz, in reproducing the properties of $MgCl_2$ in aqueous solution.

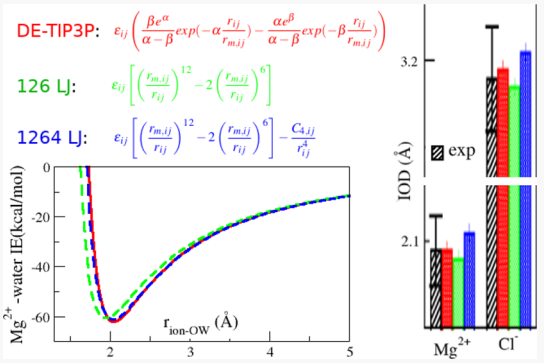

INTRODUCTION

Metal ions appear in almost half of the proteins published in protein databank (www.rcsb.org).[1,2] They carry out many important functions in the biomolecular system, particularly divalent metal ions.[3−6] The divalent metal ions, such as Mg^{2+}, Ca^{2+}, Zn^{2+}, and Mn^{2+}, can control the activity and inhibition of a protein kinase.[7] Zn^{2+} and Cu^{2+} ions can modulate the aggregation of Amyloid-β peptide, which is related to several neurodegenerative diseases.[8] In computational studies, it is essential to have good models of the ions to perform molecular dynamics (MD) simulations for the research related to the functions of these ions. Therefore, identifying suitable force field parameters, although very challenging, is of great interest.[9−24] Three main modeling methods, the bonded model,[9,12,23] the nonbonded model,[10,11,14−16] the nonbonded dummy cationic models,[13,17] have been proposed to describe metal ions in MD simulations. In the bonded model, covalent bonds or harmonic restrains between the metal and the coordinated residues/ligands are employed. The parameters of the metal-residue/ligand complex are usually generated and optimized using quantum mechanics (QM) calculation. The bonded model has advantages in reproducing highly accurate crystal structures. However, because of the predefined bonds, the model is limited in simulating the phenomena of ligand exchange and coordination number (CN) changes. On the other hand, in the nonbonded model, an ion is simply described as a point charge, and the interactions between the ion and surrounding particles are only represented by Coulombic and van der Waals (VDW) potentials. The nonbonded models allow the CN flexibility and ligand switching. However, it may be inadequate to simulate the system containing more than one metal ion in one active site. The nonbonded dummy cationic model is similar to the nonbonded model except that the metal core is surrounded by covalently bonded dummy charge atoms.[13,17] Besides the aforementioned models, there are also several polarized force field models which have been developed to incorporate charge transfer and polarization effects.[18−22]

The nonbonded model has been widely used in MD simulation because of its simplicity. Given a standard Lennard-Jones (LJ) potential, it requires the determination of only VDW radius (R_{min}) and the well depth (ε) parameters. For the sake of convenience, we use the term "VDW parameters" to refer R_{min} and ε. In 1995, VDW parameters of Zn^{2+} were determined by Stote and Karplus.[24] The development was

Received: December 8, 2020
Published: January 27, 2021

https://dx.doi.org/10.1021/acs.jctc.0c01267
J. Chem. Theory Comput. 2021, 17, 1086−1097

based on fitting the Zn^{2+}−water QM potential energy surface and reproducing the experimental first peak of the ion−oxygen distance (IOD) and hydration free-energy (HFE) values. In 2013, Li et al. performed a rational design of particle mesh Ewald (PME) compatible Lennard-Jones parameters for 16 divalent metal ions.[14] They scanned (R_{min},ε) space with targeted properties including the HFE, IOD, and CNs. However, with specific determined parameters for an ion, they could not reproduce all the experimental HFE and IOD values of the ion, simultaneously.[14] Thus, they designed three separate sets of parameters, namely HFE, IOD, and compromise (CM) sets. The HFE and IOD sets were for reproduction of experimental HFEs and IOD values, respectively, while the CM set represented a compromise between HFE and IOD properties. Afterward, Li and Merz introduced a new 12-6-4 LJ-type model in which an r^{-4} term was added into the standard LJ nonbonded potential. The introduction of the r^{-4} term enables the 12-6-4 LJ potential to better describe the ion-induced dipole interaction[15] as such the new LJ model is ideal to study a highly charged system. Thus, using the new model, they were enabled to determine an ideal parameter set that can reproduce both experimental HFE and IOD properties simultaneously.[15] On the other hand, using the nonbonded dummy cationic model, Jiang et al. determined the VDW parameters of 11 divalent metal ions without adding any extra potential term.[17] Although the nonbonded 12-6-4 LJ and nonbonded dummy cationic models showed the aforementioned achievements, the complication in use is their limitation.

In MD simulation for periodic boundary systems, lattice sum methods are usually applied for long-range interaction calculation. However, it is difficult to compute an accurate summation over all lattice images. The PME method was developed to improve the calculation efficiency of the long-range electrostatic interaction.[25,26] Nowadays, PME is the most popular method been applied in MD simulations and implemented into MD simulation software. For VDW potential, the calculation is complicated by the diversity of atom sizes. On the other side, the lattice sum methods exaggerate the symmetry effect imposed by periodic boundary conditions (PBC), resulting in unwanted long-range correlation artifacts[27] as well as anisotropy effect due to the artificially induced periodicty.[28] To overcome these artifacts, we developed the isotropic periodic sum (IPS) method to calculate long-range interactions.[29] Instead of summing over discrete PBC images as in lattice sum methods, this method uses so-called isotropic periodic images to represent remote structures statistically. The sum of interactions with the isotropic periodic images can be solved analytically and can be calculated efficiently as an additional pairwise term, which we call the IPS potential. To further simplify the application of the IPS method, we proposed a homogeneity condition,[30] which requires that the sum of interaction energies for any particle is independent of cutoff distances for a truly homogeneous system. Using the homogeneity condition, one can avoid the complicated mathematic work to solve analytic solutions of IPS and can instead make use of simple functions for IPS potentials. Recently, we also proposed a double exponential (DE) potential for repulsive and VDW attractive interactions to overcome certain drawbacks of existing function forms, such as LJ potential which has limitation on accurately fitting the properties of a real material.[31] The repulsive and attractive function form of DE is presented by eq 4 in the following Methods section. A DE potential is identified by the exponential parameters, the steepness of the repulsive interaction (α), and the decay of the attraction (β) (eq 4). The advantages of the DE potential are as follows: (i) it already includes a softcore characteristic, which make it convenient for free-energy calculation through perturbation; (ii) it converges faster than the LJ potential since the exponential functions decay faster than power functions; and (iii) the exponential parameters, α and β, can be adjusted continuously to mimic many potential functions including LJ ones.[31] Moreover, we have implemented both IPS method and DE potential for MD simulation into AMBER package.[32]

In this work, we developed a DE potential to describe repulsive and VDW interactions for divalent ions in TIP3P water. We believed that DE potential is also capable of describing the charge-induced dipole interaction as the 12-6-4 LJ potential does. Therefore, we chose divalent ions, which Li and Merz applied the 12-6-4 LJ potential for obtaining the ideal parameter set first, to test the advantages of DE potential. We first scanned the α and β DE parameter space to identify the DE potential which is compatible with the TIP3P water model for reproducing experimental water properties. We found that the identified DE potential (namely DE-TIP3P) with the parameters, α = 18.7 and β = 3.3, can best reproduce key experimental properties via the TIP3P water model. Using DE-TIP3P potential, we carried out a scanning for the (R_{min}, ε) parameter space to determine an ideal VDW parameters of 15 divalent metal ions in conjunction with TIP3P water and DE-TIP3P potential. Our DE-TIP3P potential along with the TIP3P water model achieved comparable performance as the 12-6-4 LJ model by Li and Merz[15] and the nonbonded dummy cationic models by Jiang et al.[17] in terms of reproducing experimental HFE, IOD, and CN values of 15 divalent ions, simultaneously. This work is the first steps for opening the applications of the DE functional form to model repulsive and VDW attractive interactions for its obvious advantages over LJ potentials.

METHODS

Potential Function for Nonbonded Interactions. The potential function, $U(r_{ij})$, employed for nonbonded interactions between two atoms (i,j), consists of a Coulomb term, $U_{ij}^{elec}(r_{ij})$, and a repulsive-VDW term, $U_{ij}^{repulsive\text{-}VDW}(r_{ij})$ (eq 1).

$$U(r_{ij}) = U_{ij}^{elec}(r_{ij}) + U_{ij}^{repulsive\text{-}VDW}(r_{ij}) \quad (1)$$

The Coulomb potential is calculated by eq 2.

$$U_{ij}^{elec}(r_{ij}) = \frac{e^2 Q_i Q_j}{r_{ij}} \quad (2)$$

where r_{ij} is the distance between two atoms and e is the proton charge, while Q_i and Q_j are the point charges of the two particles. For the case of LJ potential, the repulsive-VDW function is following

$$U_{ij}^{repulsive\text{-}VDW}(r_{ij}) = \varepsilon_{ij}\left[\left(\frac{r_{m,ij}}{r_{ij}}\right)^{12} - 2\left(\frac{r_{m,ij}}{r_{ij}}\right)^{6}\right] \quad (3)$$

where $\varepsilon_{i,j}$ and $r_{m,ij}$ are the well depth and the distance between two atoms at their lowest potential energy, respectively. For the DE functional form, the repulsive-VDW potential is calculated by eq 4.[31]

https://dx.doi.org/10.1021/acs.jctc.0c01267
J. Chem. Theory Comput. 2021, 17, 1086−1097

$$U_{ij}^{\text{repulsive-VDW}}(r_{ij}) = \varepsilon_{ij}\left[\frac{\beta e^{\alpha}}{\alpha-\beta}\exp\left(-\alpha\frac{r_{,ij}}{r_{m,ij}}\right) - \frac{\alpha e^{\beta}}{\alpha-\beta}\exp\left(-\beta\frac{r_{,ij}}{r_{m,ij}}\right)\right] \quad (4)$$

where the exponential parameters, α and β, define the steepness of the repulsive interaction and the decay of the attraction, respectively. With α and β been determined, a DE potential is defined. In the AMBER force field,[33] the parameters, $\varepsilon_{i,j}$ and $r_{m,ij}$, follow the Lorentz−Berthelot combining rules (eqs 5 and 6).

$$r_{m,ij} = \frac{r_{m,ii} + r_{m,jj}}{2} = R_i + R_j \quad (5)$$

$$\varepsilon_{ij} = \sqrt{\varepsilon_i \varepsilon_j} \quad (6)$$

where R_i is $\frac{r_{m,ii}}{2}$. For the convenience purpose, the default units of R and ε in this study are Å and kcal/mol, respectively.

Simulation Systems. For the molecular simulations in this work, the nonbonded interactions were either calculated by PME or IPS methods; the electrostatic interaction was described by the Coulomb potential function, and the repulsive-VDW interaction was either described by the LJ or DE potential function. In this study, the combinations of the long-range interaction method and repulsive-VDW potential function employed for the nonbonded interactions included PME-LJ for PME coupled with LJ potential, IPS-LJ for IPS coupled with LJ potential, and IPS-DE for IPS coupled with DE potential functions. All simulations were performed by using the AMBER 19 suite programs.[32] Two types of MD systems were studied. The first one, water system, contains 1584 TIP3P water molecules in a cubic box with a size of 40 Å. The second one, ion-water system, contains an ion or dummy atom solvated by 1607 TIP3P water molecules in a cubic box with a size of around 42 Å. The closest water molecule is about 1 Å away from the ion or dummy atom. Both types of systems underwent the following simulations step-by-step. First, the system underwent 1000-step steepest descent minimization followed by 1000-step conjugate gradient minimization. Next, the MD system was gradually heated up from 0 to 300 K during a 500 ps NVT (constant number, volume and temperature) simulation and equilibrated by a 3-ns NPT (constant number, volume and pressure) simulation at 300 K and 1 atm. After the system reached equilibrium, MD snapshots were collected at a frequency of one every 1 ps for the post analysis. In all the simulations, periodic boundary conditions in cubic boxes were applied, and the cutoff of 1 nm was employed for long-range interaction calculation. The lengths of sampling simulations differed from job to job and would be presented in the corresponding sections.

Hydration Free-Energy Calculation. The thermodynamic integration (TI) method,[34−37] which calculates the free-energy change between two different states of a system, was used to estimate the HFE. In the TI method, a mixed Hamiltonian $V(\lambda)$ between the initial and final states, as shown in eq 7, was used for the MD simulations

$$V(\lambda) = (1-\lambda)V_0 + \lambda V_1 \quad (7)$$

where λ is defined as a coupling parameter ranged from 0 and 1 and the potential energy $V(\lambda)$ varies from the energy of the initial state (V_0) for $\lambda = 0$ to the energy of the final state (V_1) for $\lambda = 1$. The free-energy difference is the integration of the derivative of $\partial V/\partial\lambda$ (eq 8). In this work, the final free-energy difference was obtained by employing the Gaussian quadrature formula (eq 9)[32,38] with a nine-window TI simulation λ scheme. The derivative of $\partial V/\partial\lambda$ of a snapshot obtained in a λ_i simulation was calculated by eq 10. Here, V_1 and V_0 are potential energies of the snapshot at the states $\lambda = 1$ and $\lambda = 0$, respectively.

$$\Delta G = G(\lambda=1) - G(\lambda=0) = \int_0^1 \langle \partial V/\partial\lambda \rangle_\lambda \, d\lambda \quad (8)$$

$$\Delta G = \sum_i w_i \left\langle \frac{\partial V}{\partial\lambda} \right\rangle_i \quad (9)$$

$$\frac{\partial V}{\partial\lambda} = V_1 - V_0 \quad (10)$$

The nine λ_i (i = 1, 2,...9) values were chosen as 0.01592, 0.08198, 0.19331, 0.33787, 0.5, 0.66213, 0.80669, 0.91802, and 0.98408. The weights (w_i) corresponding to the λ_i values were 0.04064, 0.09032, 0.13031, 0.15617, 0.16512, 0.15617, 0.13031, 0.09032, and 0.04064. The HFE of an ion was calculated using the thermodynamic cycle (Scheme 1). At first,

Scheme 1. Thermodynamic Cycle for the HFE Calculation

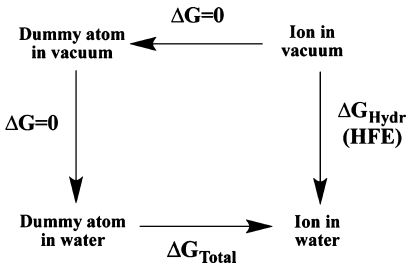

the last snapshot of the 3 ns NPT MD simulation in the equilibrium phase was used as the initial structure for a 2.5 ns NPT simulation for the first λ window ($\lambda = 1$, named λ_{10}), and a 2.5 ns NPT simulation for the window λ_i ($i < 10$) began from the snapshot at 1 ns of the λ_{i+1} NPT simulation. Note that, in this study, the $\lambda = 0$ is the state when the ions disappear in the simulation system, while $\lambda = 1$ is the state when the ions completely appear. The HFE was calculated from the last 0.5 ns of the 2.5 ns NPT simulations.

The use of the nine-window scheme with the Gaussian quadrature formula can avoid the use of the simulation with $\lambda = 0$ or 1, which may lead to a singularity. For all λ windows of the nine-window scheme, our simulations were stable for all of the ions. To increase the accuracy of HFE statistical result, we applied the following statistic strategy. For each λ window, the distribution of the 500 $\partial V/\partial\lambda$ values was first calculated, as shown in Figure S1, and then the $\partial V/\partial\lambda$ values falling within the region of population percentage larger or equal to half of the maximum value (above the red dashed lines in Figure S1.) were used to calculate the average ($\langle\partial V/\partial\lambda\rangle$) and standard deviation ($\langle\Delta\partial V/\partial\lambda\rangle$) of $\partial V/\partial\lambda$. Note that, with this strategy employed, for each λ-window only the most probable values in the $\langle\partial V/\partial\lambda\rangle$ distribution were applied to calculate the final HFE, as such, the potential outliers due to various reasons can be filtered out and the uncertainty calculated using eq 11 is

https://dx.doi.org/10.1021/acs.jctc.0c01267
J. Chem. Theory Comput. 2021, 17, 1086−1097

Table 1. Properties of Water from Experiment and Obtained by MD Simulations of TIP3P Water System at 1 atm and 300 K Using Different VDW Models and Methods for Long-Range Interaction Calculation

	ODD (Å)	density (g/mL)	E_i (kcal/mol)	diffusion coefficient (cm^{-5}/s)
experimental	2.80[a]	0.996[b]	−9.92[c]	2.9[d]
PME-LJ	2.79 ± 0.01	0.983 ± 0.003	−9.54 ± 0.03	4.94
IPS-LJ	2.79 ± 0.01	0.982 ± 0.003	−9.54 ± 0.03	5.03
DE-Wu	2.78 ± 0.01	0.964 ± 0.003	−9.35 ± 0.03	5.22
DE-TIP3P	2.79 ± 0.01	0.994 ± 0.003	−9.76 ± 0.03	4.82

[a]The data from ref 43. [b]The data from ref 44. [c]The experimental value of intermolecular energy, E_i, was from ref 45. [d]The data from ref 46.

reduced. The uncertainties of all of the HFEs calculated in this work were all smaller than 1.1 kcal/mol.

$$\Delta\Delta G = \sum_i w_i \Delta\langle \partial V/\partial\lambda_i\rangle \tag{11}$$

IOD, CN, and RDF Calculation. For the ion-water systems, we used 2000 snapshots collected from the last 2 ns of the 2.5 ns NPT simulations to calculate IOD in the first solvation shell and CNs with the same protocol as described in a previous work by Li and Merz.[14] Predictive index (PI), which was proposed and well defined in previous studies,[39,40] was applied to compare how well the VDW radius parameters from our and previous studies correlated with the revised effective ionic radii by Shannon.[41] For HEF and IOD, we also calculated relative errors, which is defined as the percentage of the unsigned error between the calculated and experimental values to the experimental value, to compare the performance of different models. For the TIP3P water system, we calculated the density, the self-diffusion constant, the radial distribution function (RDF) of oxygen−oxygen and the oxygen−oxygen distance (OOD) in the first solvent shell using 2000 snapshots collected from the last 2 ns of 5 ns NPT simulations. Of note, OOD was calculated using the similar method for calculating IOD of an ion-water system.

Diffusion Calculation. To calculate the diffusion of water and ions, we performed twenty 5 ns NPT simulations for each system. The initial conformation was the last snapshot of the NPT simulation for OOD/IOD calculation. The self-diffusion coefficient of water and diffusion coefficients of ions in aqueous solution were calculated using an ensemble-average method described elsewhere.[42] In brief, the mean of mean-square-displacements (MSD) was calculated by running average of MSD of 20 MD trajectories, then the slope of mean MSD to simulation time was estimated by a least-square fitting, and the diffusion coefficient D was calculated using eq 12.

$$D = \frac{\langle |\bar{r} - \bar{r^0}|^2\rangle}{6t} \tag{12}$$

RESULTS AND DISCUSSION

Effect of Long-Range Interaction Methods on TIP3P Water Simulation. The current implementation of the DE-related code allowed us to use DE potential in conjunction of the IPS method in MD simulations. Therefore, we carried 5 ns NPT simulations for the water system for both PME-LJ and IPS-LJ nonbonded schemes to investigate whether two long-range interaction methods, PME and IPS, differ from each other. As listed in Table 1, the OOD, density, total potential, and self-diffusion constant of TIP3P with PME-LJ and IPS-LJ were almost identical (Table 1). Additionally, the oxygen−oxygen RDFs of the TIP3P from PME-LJ and IPS-LJ simulations were perfectly overlapped (Figure 1). Therefore, the nonbonded interactions are independent to the long-range interaction methods.

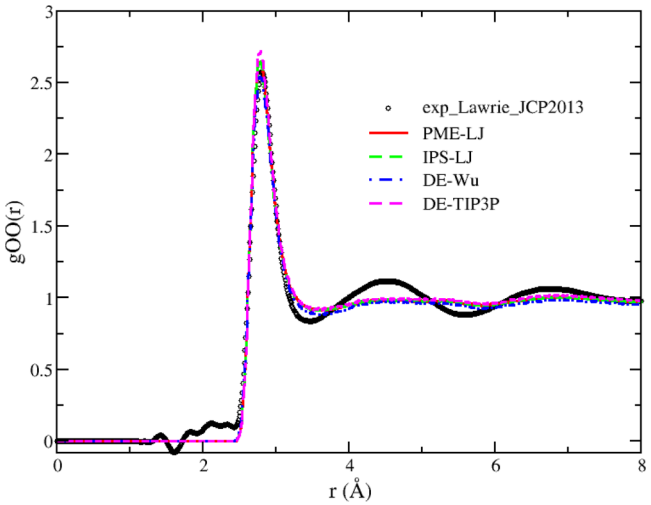

Figure 1. Oxygen−oxygen RDF of TIP3P waters in different potentials employed to nonbonded interactions.

DE α and β Parameters for TIP3P Water. In a previous report by Wu and Brooks, it was found that the DE potential with α = 17.47 and β = 4.1 can reproduce the LJ potential very well.[31] This DE potential was named as DE-Wu thereafter for the sake of convenience. As demonstrated in Figures 2a,b, the repulsive and VDW attractive interaction energies ($U_{ij}^{\text{repulsive-VDW}}$) of two TIP3P water molecules calculated by the LJ and DE-Wu potentials were very similar. Note that the well depth of hydrogen atoms in the TIP3P water model is 0 kcal/mol and $U_{ij}^{\text{repulsive-VDW}}$ is purely from the interactions between the two oxygen atoms. However, the TIP3P water properties obtained from the 5 ns NPT simulation using DE-Wu were quite different from those obtained from the simulation using the LJ potential (Table 1). Despite the oxygen−oxygen RDF [gOO(r)] and its first peak position of the TIP3P were similar for the two potential models, the density and intermolecular energy (E_i) from those simulations are significantly different. Considering both the simulations were performed at the same conditions, the differences of water properties obtained from the simulations are therefore originated from the difference between the LJ and DE-Wu potential at the region of $R_{\min}/2 < r < R_{\min}$ (Figure 2c). According to Table 1, DE-Wu potential was not as good as the LJ potential in reproducing key water liquid properties in conjunction with the TIP3P water model. Our result indicated that although the overall shape of the two potentials is

https://dx.doi.org/10.1021/acs.jctc.0c01267
J. Chem. Theory Comput. 2021, 17, 1086−1097

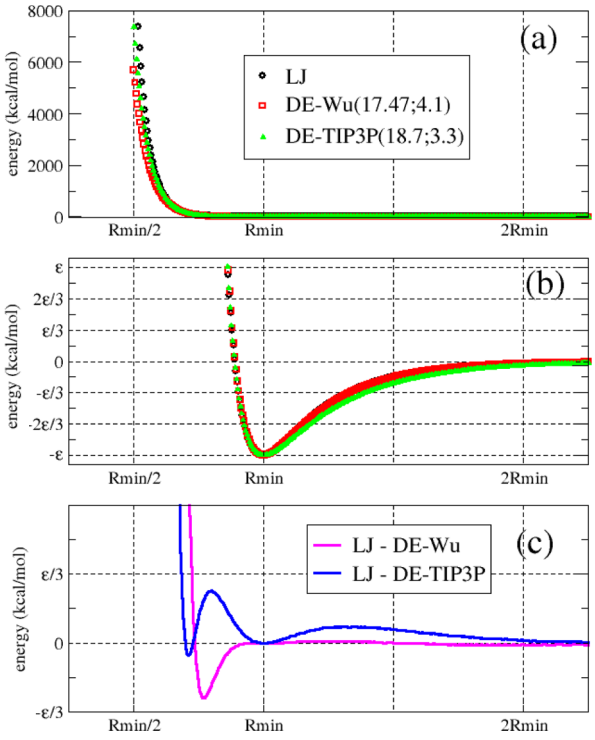

Figure 2. Repulsive and VDW attractive interactions ($U_{ij}^{\text{repulsive-VDW}}$) of two TIP3P water molecules (i and j), which were calculated by using DE-Wu and De-TIP3P potentials. (a) General view. (b) Close view around the potential well. (c) Energy differences between LJ and DE-Wu potentials (magenta line) and LJ and DE-TIP3P potentials (blue line). Here, ε is the well depth and R_{min} is the distance between two oxygen atoms at their lowest potential energy. In the TIP3P water model, the values of R_{min} and ε are 3.5366 Å and 0.152 kcal/mol for oxygen, while they are zero for hydrogen atoms.

essentially similar, the subtle difference around the R_{min} area can cause significantly different simulation results. Our first task is therefore to identify a set of α and β parameters of DE potential which can well reproduce the experimental values of water density, OOD, and first peak location of RDF for the TIP3P water model.

Using a step 0.2, the α and β parameters were scanned in ranges from 15.1 to 21.1 and from 2.5 to 5.5, respectively. In total, there were 31 values of α and 16 values of β resulting 496 (α, β) combinations. Again, the density and OOD distribution function of the water were calculated from the last 2 ns of the 5ns NPT ensemble for each (α, β) pair. The dependence of the OOD and density of TIP3P water on the α and β parameters are illustrated by Figure 3a,b. The surfaces of the OOD and the density were reproduced by using 2D cubic spline interpolation with MATLAB software.[47] The contour curves at experimental values of the first OOD peak position (2.79 Å) and density (0.996 g/mL) were obtained by using contour data function in MATLAB software (Figure 3c).[47] There were several intersection points between the two contour curves. We simply chose the first intersection point with α = 18.7 and β = 3.3 as the best combination, and we denoted this set of parameters, α = 18.7 and β = 3.3, as DE-TIP3P. The DE-TIP3P and LJ potentials are similar at the region of $r > 2R_{\text{min}}$, a little different at the region of $R_{\text{min}} < r < 2R_{\text{min}}$, and significantly different at the region of $r < R_{\text{min}}/2$, as indicated in Figure 2c.

The water properties, which were calculated from the NPT simulations at 300 K and 1 atm using the different potential forms with TIP3P water model, showed that DE-TIP3P simulation was much better than the other ones in reproducing water experimental values of IOD, density, and E_i (Table 1). For the OOD parameter, the calculated values, 2.78 ± 0.01 Å for DE-Wu potential and 2.79 ± 0.01 Å for the other potentials, were all in good agreement with the experimental value (2.79 Å). However, similar to the LJ potential, DE-TIP3P potential cannot reproduce the second and third peaks of the experimental gOO(r) function (Figure 1). This limitation may be due to an intrinsic problem of the water model itself. For the density, the calculated value from the DE-TIP3P simulation (0.994 ± 0.003 g/mL) was very close to the experimental value (0.996 g/mL), while the densities from other simulations were smaller than 0.99 g/mL. For intermolecular energy which is directly related to heat of vaporization, the predicted E_i from the DE-TIP3P simulation, −9.76 ± 0.03 kcal/mol was again much better reproducing the experimental value (−9.92 kcal/mol) than other VDW potentials. Note that E_i value of TIP3P water in our PME-LJ

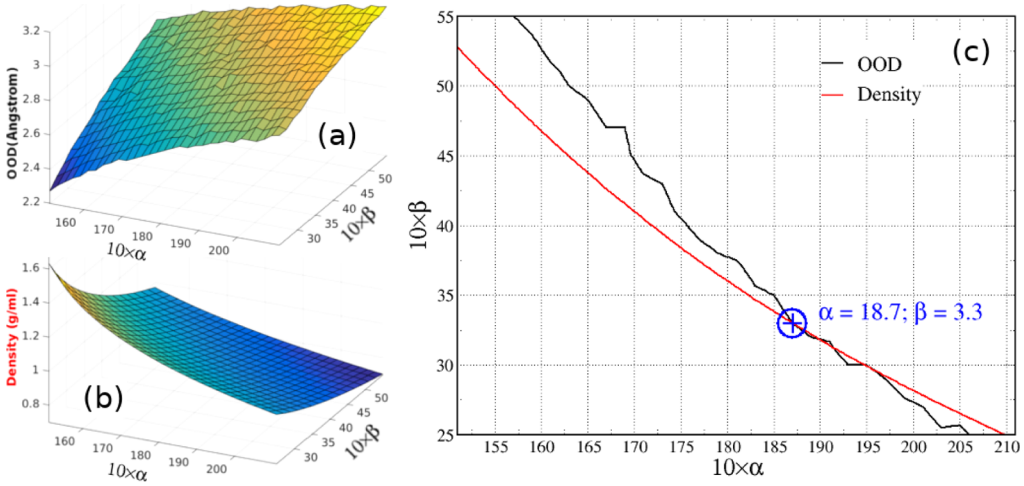

Figure 3. α and β dependence of the water OOD (a) and density (b). Panel (c) shows the contour curves for the TIP3P OOD at 2.79 Å (black line) and density at 0.996 g/ml (red line) and their intersection point at (α = 18.7, β = 3.3).

https://dx.doi.org/10.1021/acs.jctc.0c01267
J. Chem. Theory Comput. 2021, 17, 1086−1097

simulation, −9.54 kcal/mol, was different from a previous report,[45] which was −9.86 kcal/mol. We suggested that the difference may be due to the different methods applied to account for the long-range interactions. For the self-diffusion constant, the calculated values were all significantly larger than the experimental value, even though DE-TIP3P achieved the best prediction performance (Table 1).

Determination of Divalent Metal Ions' VDW Parameters to Be Compatible with TIP3P Water and DE-TIP3P. *Scanning the Ion VDW Parameters, R and ε.* To derive the VDW parameters of the divalent metal ions, which are compatible with TIP3P water and DE-TIP3P, we performed the coarse-grained and fine-grained scans sequentially. In the coarse-grained scan, a dummy atom bearing +2 charge was applied and the mass of the dummy atom in the ion-water system was set to be 64 g/mol. Note that the choice of mass has a limited influence on the simulated HFE and RDF of the metal ion-water system.[14] There were 330 combinations of 22 R values (R = 0.1:0.1:2.2) and 15 ε values (ε = 0.0001, 0.001, 0.01, 0.1, 1, 3, 5, 7, 10, 15, 25, 50, 100, 200, and 400) to be considered. For each combination, we carried out the simulations of the ion-water system and calculated the HFE, IOD, and CN values, as described in the Methods section. The surfaces of HFE and IOD in the (R, $-\log(\varepsilon)$) space were constructed with 2D cubic spline interpolation using MATLAB software.[46] For each metal ion with given experimental HFE and IOD values, the HFE and IOD contour curves at the experimental values were determined and plotted on one (R, $-\log(\varepsilon)$) graph. The crossing point (R_{cg}, $-\log \varepsilon_{cg}$) of the HFE and IOD curves was identified and considered as a center point in the next fine scan.

In the followed fine-grained scans, for each metal ion with (R_{cg}, $-\log \varepsilon_{cg}$) determined in the coarse-grained scan, we scanned the parameter space of $R \in [R_{cg} - 0.1, R_{cg} + 0.1]$ and $\varepsilon \in [\varepsilon_{cg} - \delta\varepsilon_{cg}, \varepsilon_{cg} + \delta\varepsilon_{cg}]$, where $\delta\varepsilon_{cg}$ was $\varepsilon_{cg}/10$ for $\varepsilon_{cg} \leq 10$, $\varepsilon_{cg}/20$ for $\varepsilon_{cg} \in (10,50]$, $\varepsilon_{cg}/30$ for $\varepsilon_{cg} \in (50,110]$, and $\varepsilon_{cg}/50$ for $\varepsilon_{cg} > 110$. In total, 121 parameter pairs, a combination of 11 R values and 11 ε values, were considered. For R parameter, the step size is 0.02, whereas the step size of ε is $\delta\varepsilon_{cg}/5$. Similar to the coarse-grained scan, for each (R,ε) combination, we performed simulations of the ion-water system and calculated HFE, IOD, and CN quantities. Unlike the coarse-grained scan, the exact mass of the metal ion was applied in fine-grained simulations. Again, we constructed the surfaces of HFE and IOD in the (R,ε) space and the HFE and IOD contour curves using the corresponding experimental values. Finally, the VDW parameters, R and ε, of the ion was identified from the intersection point of the HFE and IOD contour curves.

The two scan schemes provided the balance between number of the simulations needed and accuracy of the VDW parameter determination. The coarse-grained scan covered a wide searching space of the R and ε parameters, and the same HFE and IOD surfaces obtained for the dummy atom were used for all ions. Thus, it can dramatically reduce the computer time and resource consumption for deriving VDW parameters of multiple ions. However, the determination of the contour curves and their intercross point may not be accurate due to the spline interpolation fittings and the use of $\log(\varepsilon)$ [a little difference of $\log(\varepsilon)$ value can lead to a significant difference of ε value]. In contrast, the fine-grained scan focused on specific small space of the VDW parameters with higher resolution and used the real mass of individual ion, eliminating the error sources in the coarse-grained scan. However, fine-grained scans are computational costly as we need to run simulations for each ion. A similar two-scan strategy were applied in a previous work by Jiang et al.[17] Li et al. also derived VDW parameters of a series of metal ions using two scanning states.[14] However, in their first scan, the considered range of ε ranges from 10^{-6} to 1, and they did not obtain the intercross points of the HFE and IOD contour curves in the considered range of ε. Instead, they applied the rules obtained from the noble gas curves to estimate the VDW parameters of ions. In the second scan, they also tuned the R and ε parameters around the values obtained in the first scan to reproduce IOD and CN experimental values. However, no detailed tuning strategy was provided, and they did not mention whether the real mass of the ions was used in the second scan or not. Figure 4 shows the case of Ca^{2+}

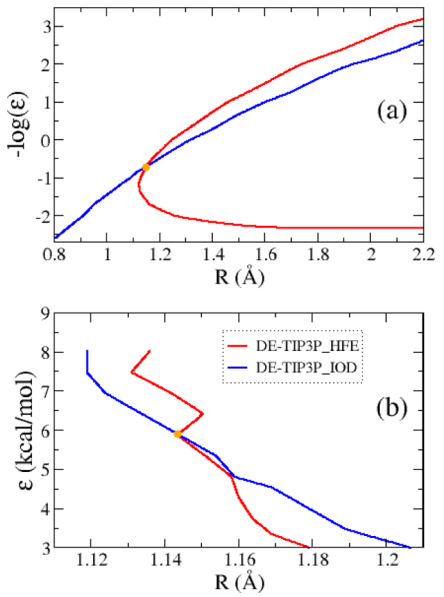

Figure 4. HFE and IOD contour curves of Ca^{2+} ion from the VDW parameter coarse-grained (a) and fine-grained (b) scans.

ion as an example in our work (similar data for the other ions are shown in Figures S2 and S3 in Supporting Information). In the coarse-grained scan (Figure 4a), we obtained R = 1.1491 and $\log(\varepsilon)$ = 0.72711 (ε = 5.3347). In the fine-grained scan (Figure 4b), the identified VDW parameters were R = 1.1437 and ε = 5.8792. As demonstrated in Figure 4b, the HFE contour curves were zigzag lines, which explained why the coarse-grained scan using $\log(\varepsilon)$ can lead to inaccurate determination of the intercross point.

VDW Parameters of Divalent Metal Ions Obtained by MD Simulations Using TIP3P Water and DE-TIP3P. The VDW parameters, R and ε, of 15 divalent metal ions, identified from above two-step scans, are listed in Table 2. Note that we could not determine the parameters for Be^{2+} ion due to the missing crossing point in the coarse-grained scan (Figure S2). For the R parameter, the values ranged from 0.464 to 1.688. Using the revised ion effective radii data by Shannon as a reference,[40] we studied how well the R parameters developed in this work and those by Li and Merz and Jiang et al.[14,17] correlated to the Shannon data. As shown in Figure 5, for any ion, the R parameter in the CM and 12-6-4 LJ parameter sets of Li and Merz's work[14,15] was much larger than the corresponding values in the parameter sets of our DE-TIP3P, Jiang et al.'s and Shannon's.[40] Our DE-TIP3P parameter set had the highest

https://dx.doi.org/10.1021/acs.jctc.0c01267
J. Chem. Theory Comput. 2021, 17, 1086−1097

Table 2. VDW Parameters, R (in Å) and ϵ (in kcal/mol), of 15 Divalent Metal Ions Obtained by MD Simulations Using the TIP3P Water Model and DE-TIP3P Nonbonded Scheme[a]

	experimental			calculated with DE-TIP3P				
ions	HFE[b]	CN	IOD	R	ϵ	HFE	CN	IOD
Cu^{2+}	−480.4	6[c]	2.11[g]	0.4856	508.65895	−480.4	6.2	2.10
Ni^{2+}	−473.2	6[c]	2.06[c]	0.4642	286.63553	−473.8	6.0	2.05
Zn^{2+}	−467.3	6[c]	2.09[c]	0.5	285.18754	−467.1	6.0	2.08
Co^{2+}	−457.7	6[c]	2.10[c]	0.5262	197.20082	−457.0	6.0	2.09
Cr^{2+}	−442.2	6[e]	2.08[e]	0.578	64.6987	−440.7	6.0	2.07
Fe^{2+}	−439.8	6[c]	2.11[c]	0.5894	98.86667	−438.8	6.0	2.10
Mg^{2+}	−437.4	6[c]	2.09[c]	0.6002	61.04789	−435.8	6.0	2.09
V2+	−436.2	6[d]	2.21[d]	0.6245	130.54407	−435.5	7.0	2.21
Mn^{2+}	−420.7	6[c]	2.19[c]	0.6849	53.98914	−420.1	6.7	2.19
Hg^{2+}	−420.7	6[c]	2.41[c]	0.8182	188.89922	−420.4	8.1	2.42
Cd^{2+}	−419.5	6[c]	2.30[c]	0.719	97.55051	−421.0	7.8	2.31
Ca^{2+}	−359.7	8[f]	2.46[f]	1.1437	5.87921	−360.2	8.0	2.46
Sn^{2+}	−356.1	6[e]	2.62[c]	1.1698	30.63429	−354.8	9.0	2.62
Sr^{2+}	−329.8	8[e]	2.64[c]	1.4134	2.8488	−328.6	8.8	2.63
Ba^{2+}	−298.8	9[g]	2.83[g]	1.688	1.92911	−299.3	9.2	2.83
SD						**0.89**	**1.14**	**0.008**

[a]The experimental and calculated values of HFE (in kcal/mol), IOD (in Å), and CN for the developed parameters are listed. The standard deviation (SD) was obtained by treating the corresponding experimental values as the true values. [b]From ref 48. [c]From ref 49. [d]From ref 50. [e]From ref 51. [f]From ref 52. [g]From ref 53.

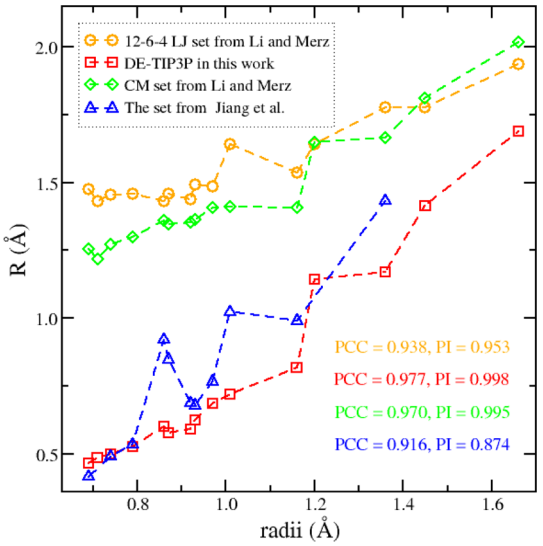

Figure 5. Correlation between Shannon's revised effective ion radii and the R parameters of the four VDW models, including 12-6-4 LJ from Li and Merz, DE-TIP3P (this work), the TIP3P CM set by Li and Merz, and the TIP3P set by Jiang et al. The PCC and PI for each comparison are shown.

Pearson correlation coefficient (PCC) and PI than the VDW parameter sets from the previous studies. This result indicated that our determined R parameters were more consistent with the Shannon revised effective radii. For the ϵ parameter, the identified values of our TIP3P-DE set varied from 1.93 kcal/mol for Ba^{2+} to 508.66 kcal/mol for Cu^{2+}. The range of the ϵ parameter values was much larger than that of the Jiang et al.'s set for their nonbonded dummy cationic model, for which the ϵ parameter ranged from 0.2 to 100.7 kcal/mol. Unlike ours and Jing et al.'s, the ϵ values of the CM and 12-6-4 LJ sets for TIP3P water by Li and Merz[14,15] were smaller than 1 kcal/mol. Apparently, the magnitude of the ϵ values strongly depends on the model and functional form describing the VDW interactions.

Evaluation of the DE-TIP3P VDW Parameters for Divalent Ions. To evaluate the VDW parameters of 15 divalent metal ions in our DE-TIP3P set, we first calculated HFE, IOD, and CN for each ion and compared them with corresponded experimental values. As shown in Table 2 and Figure 6, the experimental HFE and IOD properties of the ions were well represented by the DE-TIP3P parameter set. The standard deviation of HFE and IOD was 0.89 kcal/mol and 0.008 Å,

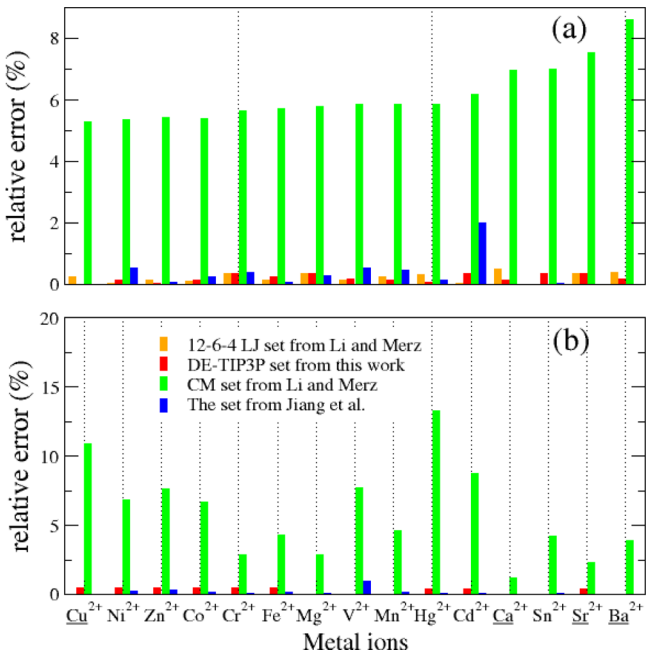

Figure 6. Relative errors of the calculated values of HFE (a) and IOD (b) for the 15 metal ions simulated with the parameters for TIP3P from this work, Li and Merz, and Jiang et al. studies.[14,15,17] The ions underlined indicate its absence in the study by Jiang et al.[17]

https://dx.doi.org/10.1021/acs.jctc.0c01267
J. Chem. Theory Comput. 2021, 17, 1086−1097

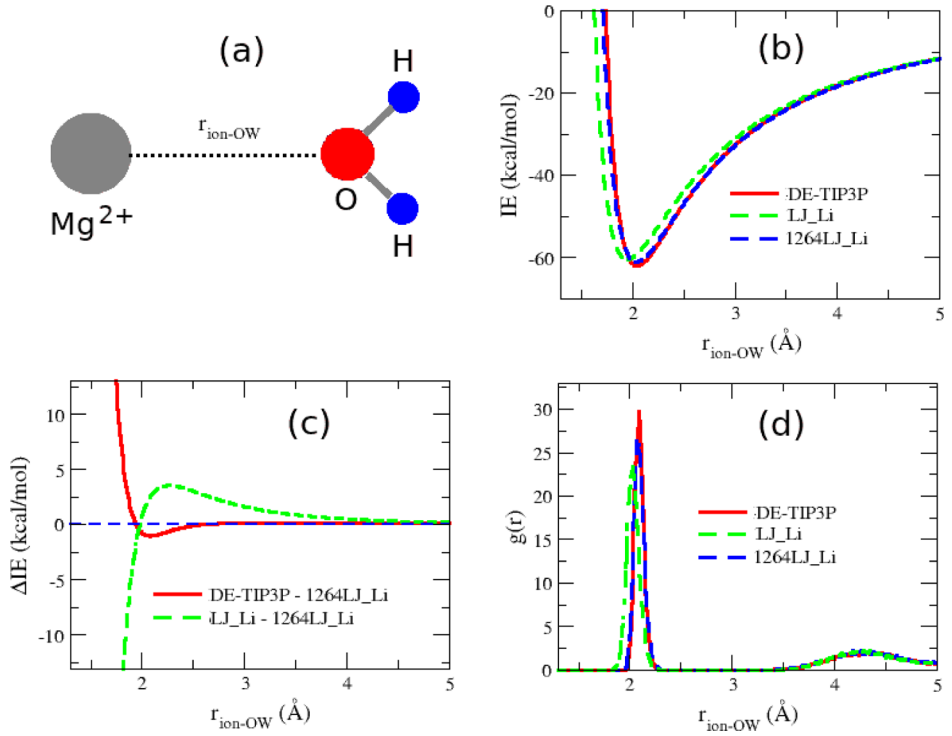

Figure 7. Nonbonded interactions between Mg^{2+} and TIP3P water. (a) Cartoon representation of Mg^{2+}−water interaction; (b) interaction energies (IE) between Mg^{2+} and water by three different VDW models, namely, DE-TIP3P (this work), LJ (CM set, Li and Merz),[14] and 12-6-4 LJ (Li and Merz);[15] (c) IE difference using the energies of 12-6-4 LJ model as the reference. The blue dashed line is for ΔIE = 0; (d) the ion−oxygen RDFs of the Mg^{2+}−water system.

respectively. All HFE and IOD relative errors obtained from the DE-TIP3P set were lower than 1% (Figure 6). For the CN property of the ions, the DE-TIP3P sets can reproduce the experimental CN values for Cu^{2+}, Ni^{2+}, Zn^{2+}, Co^{2+}, Cr^{2+}, Fe^{2+}, Mg^{2+}, Ca^{2+}, and Ba^{2+} ions. However, it could not reproduce the experimental CN values for V^{2+}, Mn^{2+}, Hg^{2+}, Cd^{2+}, Sn^{2+}, and Sr^{2+} ions. We made comparisons on reproducing the experimental HFE and IOD data between our DE-TIP3P nonbonded parameter set and the other three popular parameter sets, that is, Li and Merz's compromise nonbonded model for the TIP3P water model (the CM set),[14] Li and Merz's 12-6-4 LJ nonbonded model for the TIP3P water model,[15] and Jiang et al.'s nonbonded dummy cationic model set.[17] As shown in Figure 6, it is obvious that the performance of the DE-TIP3P model was comparable with the complicated nonbonded dummy cationic model and 12-6-4 LJ nonbonded model but outperformed the CM parameter set.[14] However, in terms of CN, for some ion cases, the nonbonded dummy cationic models from Jiang et al. were better than our and Li and Merz ones (Figure S4). Interestingly, the CN values of the metal ions obtained using our DE-TIP3P parameter set were almost the same as the those obtained from 12-6-4 LJ models by Li and Merz (Figure S4).[15]

In a previous work,[14] Li and Merz could not get the ideal parameters for the nonbonded models of the divalent ions with the standard LJ potential. Afterward, they introduced a $1/r^4$ term to the standard LJ potential to develop the so-called 12-6-4 LJ potential for modeling the interaction between metal ions and waters. It is noted that the 12-6-4 LJ potential did not apply to the nonbonded water−water interaction. The new 12-6-4 LJ potential enabled them to determine an ideal parameter set which could perfectly reproduce the experimental properties of the divalent metal ions, suggesting that their 12-6-4 LJ and Coulombic potentials could describe the nonbonded interaction between the metal ions and water molecules very well. Therefore, we next compared our DE-TIP3P set, the CM set, and 12-6-4 LJ set for TIP3P simulations from Li et al.'s studies[14,15] on modeling the ion-water nonbonded interaction. Figure 7b shows the interaction energy between a water molecule and Mg^{2+} ion models from the DE-TIP3P set and Li and Merz's CM and 12-6-4 LJ sets. It is obvious that the ion-water interaction energies calculated using our DE-TIP3P models were very similar to those by using the 12-6-4 LJ model, but significantly different from the CM model. We further calculated the energy differences by subtracting the energies of the 12-6-4 LJ model from those of our model and the CM model. As shown in Figure 7c, the difference between our model and the 12-6-4 model was negligible when the ion−water oxygen distance is larger than 2.5 Å. The energy of our model was lower when the ion−water oxygen distance was between 1.94 and 2.5 Å but significantly higher between 1.275 and 1.94 Å. When the ion-water oxygen is smaller than 1.275 Å, the energy of our model became more negative again (Figure S5). On the contrary, the interaction energy difference of the CM model was much larger than the one of the DE-TIP3P model in the distances, where gOO(r) has significant distribution (Figure 7d). The result for other divalent metal ions in term of the ion-water interaction energy was similar to the Mg^{2+} case (Figure S6).

To further test our nonbonded models, we carried on the simulations of $MgCl_2$ at different concentrations, including 0.25, 0.5, and 1 M, in TIP3P waters. The parameters of Mg^{2+} ions came from our DE-TIP3P set. The force field parameters of Cl^-, 2.56295 Å for R and 0.03763 kcal/mol for ε, were obtained by using the same scanning scheme as described above. The compositions of the three MD simulation systems

https://dx.doi.org/10.1021/acs.jctc.0c01267
J. Chem. Theory Comput. 2021, 17, 1086−1097

are listed as follows: 0.25 M (10 Mg^{2+} and 20 Cl^- solvated in a cubic water box with 2157 water molecules), 0.5 M (19 Mg^{2+}, 38 Cl^-, and 2185 water molecules), 1 M (38 Mg^{2+}, 76 Cl^-, and 2102 water molecules). Those systems were similar to those used by Li and Merz in the previous work.[15] Our post-analysis for the aqueous $MgCl_2$ systems showed that the IOD values of Mg^{2+} and Cl^- were 2.09 and 3.19 Å in all $MgCl_2$ concentration systems, respectively. Those values were in excellent agreement with the experimental data, 2.09 ± 0.04 Å for Mg^{2+} and 3.18 ± 0.06 Å for Cl^-, reported by Marcus.[49] In the previous work by Li and Merz for the same aqueous $MgCl_2$ system, the IOD values of Mg^{2+} and Cl^- were 2.08 and 3.17 Å when using the CM model and 2.11 and 3.21 Å when using the 12-6-4 LJ model.[15] Therefore, the IOD values for Mg^{2+} and Cl^- predicted by the DE-TIP3P model are better or comparable to those by Li and Merz's models.

Finally, we performed simulations to calculate the diffusion coefficients of Mg^{2+} and Zn^{2+} using the three non-bonded models, which are DE-TIP3P, CM LJ-TIP3P, and 12-6-4 LJ-TIP3P. The diffusion was calculated using the equations described in the previous work by Shavkat Mamatkulov and Nadine Schwierz.[54] Our result showed that the calculated diffusion coefficients of both cations were comparable for all three models. For Mg^{2+}, the diffusion coefficient was 0.569 × 10^{-9}, 0.546 × 10^{-9}, and 0.519 × 10^{-9} m^2 s^{-1}, for DE-TIP3P, CM LJ-TIP3P, and 12-6-4 LJ-TIP3P, respectively. Those values were close to 0.705 10^{-9} m^2 s^{-1}, the experimental value.[54] Similarly, the calculated diffusion coefficients of Zn^{2+}, 0.662 × 10^{-9}, 0.672 × 10^{-9}, and 0.645 × 10^{-9} m^2 s^{-1} for the three corresponding models, were also close to 0.715 10^{-9} m^2 s^{-1}, the experimental value.[55]

Future Developments of DE Potential. VDW interactions between two particles are usually described by a LJ potential which consists of a repulsive term (r^{-12}) for describing Pauli repulsion at short ranges due to overlapping electron orbitals and an attractive term (r^{-6}) for representing attraction at long ranges (eq 3). For two particles, i and j, the potential shape is defined given a set of $R_{min}(r_{m,ij})$ and ε (ε_{ij}) values. Here, the R_{min} indicates the position where the repulsive and attractive forces are balanced, while ε relates to how strong the VDW interaction between two particles. The dispersion in the form of $1/r^6$ is based on a pair of atoms with instantaneous induced dipoles. However, in real systems many factors would result in different functional forms. For example, instantaneous induced multipole interactions, such as charge−dipole, charge−quadrupole, and dipole−quadrupole interactions, may also contribute to dispersion, which will deviate from the $1/r^6$ form. In bulk systems, many body interactions also play important roles that may not be best described by the $1/r^6$ form. For infinite systems, long-range interactions are factorized into the pairwise potential in the IPS method and the reaction field methods, as a result, the pairwise potentials are no longer in their original functional forms. With so many factors affecting the potential functional form, the exponential function provides a convenient way to account for the deviations. With a fixed functional form of $1/r^6$, even combined with $1/r^4$, it is difficult to account for so many factors.

Similar to a LJ potential, the DE potential also includes a repulsive and an attractive terms, $\varepsilon_{ij}\frac{\beta e^{\alpha}}{\alpha-\beta}\exp\left(-\alpha\frac{r_{,ij}}{r_{m,ij}}\right)$ and $\varepsilon_{ij}\frac{\alpha e^{\beta}}{\alpha-\beta}\exp\left(-\beta\frac{r_{,ij}}{r_{m,ij}}\right)$, and the meaning of R_{min} and ε is the same as those in the LJ potential. However, the exponential parameters (α and β), which can be adjusted, make DE to be flexible to represent the shape of potentials. Therefore, DE can take into account many interaction sources between two particles such as instantaneous charge, dipole, multipole, and their polarizable moments. This is an important advantage of the DE over other potential forms. For example, the r^{-6} term in LJ potential is only true by assuming attraction is solely due to fixed point dipole−dipole interactions, while adding r^{-4} term into 12-6 potential can account for the ion-induced dipole interaction as pointed out above.[15] Using 12-6-4 LJ form, Li and Merz have successfully developed nonbonded models for divalent ions, for which the charge-induced dipole interaction becomes very significant. Those highly charged systems are difficult to model using a LJ potential without the C4 term.[15]

To adequate sample conformations and accurate calculation of the energies of a molecular system, the molecular mechanical force field, the foundation of molecular simulation, needs to accurately model all kinds of interaction terms including polarization energy which can be explicitly calculated using a polarizable force field. However, some source of polarization energy can be described using a more complicated VDW potential function in a non-polarizable force field. For example, the ion-induced dipole interaction can be described by a C4 term in a 12-6-4 LJ potential.[15] However, applying a more complicate function form for VDW interaction may slow down sampling speed compared to the simple LJ potential. Here, we investigated how sampling performance was affected by employing the DE potential. For a MD system containing 1584 TIP3P water molecule (4752 atoms), the speeds of PME-LJ and DE-TIP3P simulations were 4.25 and 4.54 ns/day, respectively. Both MD simulations were performed with a workstation equipped with a dual Intel E5-2683 v4 @ 2.10GHz CPUs. Evidently, the simulation using IPS-DE is slightly faster than that one using PME-LJ. In contrast, applying a polarizable force field which explicitly calculates that polarization energy can dramatically slow down sampling speed. For instance, a GTX1080 GPU can sample 42.9 ns/day for a system containing 408,609 atoms applying AMBER additive force field and PME-LJ (https://ambermd.org/GPUPerformance.php), but it can only sample 2.3 ns/day for a system containing 388,783 atoms using the Drude polarizable force field.[56] In conclusion, applying DE potential can describe some interactions due to polarization at a minimal cost. Currently, the DE potential was only implemented in the CPU version of the pmemd program (both serial and parallel versions) in AMBER software package, we plan to implement the DE potential form to the GPU version of the pmemd program.

It is an attractive idea to apply a general functional form like DE to resemble different combinations of LJ terms (such as 12-6 LJ and 12-6-4 LJ) by utilizing different α and β parameters. In this study, we have demonstrated that the DE functional form can very well resemble the 12-6 LJ potential for TIP3P water and the 12-6-4 LJ potentials for a set of divalent ions. Encouraged by these results, we are in a procedure of developing a spectrum of DE-based force fields for water, ions, organic molecules, and so forth, and the results will be reported later. Still there are several quick applications to utilize the capabilities of the DE potential, beyond what is presented in this study. One idea, to assist when using the DE with older existing force field parameter sets that have been tuned for use with a VDW cutoff scheme at a particular distance, would be to implement standard shifting and

https://dx.doi.org/10.1021/acs.jctc.0c01267
J. Chem. Theory Comput. 2021, 17, 1086−1097

switching functionality to terminate DE interactions at a selected distance. This allows those parameter sets to be used without the need to significantly tune the long-range effects on density and transport properties. Another idea is to allow the use of the DE potential with force field parameter sets that have been highly tuned for use with r^{-6} LJ PME (LJ-PME).[57,58] This is carried out by incorporating the LJ-PME switching approach[59] that would allow the conversion of the DE potential at short ranges to the multiplicative r^{-6} combination rules at longer distances, in the same manner as is used in Gromacs[60] for standard additive combination rules used at short ranges. These extensions would allow the DE method to be used with most existing parameter sets without the need to significantly retune long-range VDW interactions. We plan to report on these in a future study.

CONCLUSIONS

In this work, we put the first step for the applications of a DE functional form to describe the VDW interaction for studying water-ion systems. We found that the DE-TIP3P potential with parameters α of 18.7 and β of 3.3 can reproduce water's experimental density and first peak OOD very well. We then developed the VDW parameters using the DE-TIP3P potential for 15 divalent metal ions in conjunction with the TIP3P water model. The parameter set, DE-TIP3P, achieved an encouraging performance in reproducing experimental HEF, IOD, and CN properties, which is comparable to or better than that achieved by a complicated nonbonded dummy cationic model by Jiang et al. and the 12-6-4 models by Li and Merz. In conclusion, DE is an attraction functional form for modeling VDW interactions.

ASSOCIATED CONTENT

Supporting Information

The Supporting Information is available free of charge at https://pubs.acs.org/doi/10.1021/acs.jctc.0c01267.

Distribution of $\partial V/\partial\lambda$ at nine λ windows from the simulation with (R, ϵ) pair of (1 Å, 10 kcal/mol), HFE and IOD contour curves, CN values of the ions from DE-TIP3P and 12-6-4 LJ sets, and the ion-water interaction energy (PDF)

AUTHOR INFORMATION

Corresponding Authors

Xiongwu Wu − *Laboratory of Computational Biology, National Heart, Lung, and Blood Institute, National Institute of Health, Bethesda, Maryland 20892, United States*; Email: wuxw@nhlbi.nih.gov

Bernard R. Brooks − *Laboratory of Computational Biology, National Heart, Lung, and Blood Institute, National Institute of Health, Bethesda, Maryland 20892, United States*; Email: brb@mail.nih.gov

Junmei Wang − *Department of Pharmaceutical Sciences and Computational Chemical Genomics Screening Center, School of Pharmacy, University of Pittsburgh, Pittsburgh, Pennsylvania 15261, United States*; orcid.org/0000-0002-9607-8229; Email: junmei.wang@pitt.edu

Authors

Viet Hoang Man − *Department of Pharmaceutical Sciences and Computational Chemical Genomics Screening Center, School of Pharmacy, University of Pittsburgh, Pittsburgh, Pennsylvania 15261, United States*; orcid.org/0000-0002-8907-6479

Xibing He − *Department of Pharmaceutical Sciences and Computational Chemical Genomics Screening Center, School of Pharmacy, University of Pittsburgh, Pittsburgh, Pennsylvania 15261, United States*; orcid.org/0000-0001-7431-7893

Xiang-Qun Xie − *Department of Pharmaceutical Sciences and Computational Chemical Genomics Screening Center, School of Pharmacy, University of Pittsburgh, Pittsburgh, Pennsylvania 15261, United States*

Complete contact information is available at: https://pubs.acs.org/10.1021/acs.jctc.0c01267

Author Contributions

V.H.M., X.W., and J.W. designed the project. V.H.M. performed the simulations and analyzed data. V.H.M., X.W., X.H., X.X., B.R.B., and J.W. discussed and wrote the paper.

Notes

The authors declare no competing financial interest.

ACKNOWLEDGMENTS

This work was supported by grants R01-GM079383, R21-GM097617, and P30-DA035778 from the National Institutes of Health. The content is solely the responsibility of the authors and does not necessarily represent the official views of the National Institutes of Health or other funding organizations. Computational support from the Center for Research Computing of University of Pittsburgh and Pittsburgh Supercomputing Center (CHE180028P) is acknowledged.

REFERENCES

(1) Berman, H. M.; Westbrook, J.; Feng, Z.; Gilliland, G.; Bhat, T. N.; Weissig, H.; Shindyalov, I. N.; Bourne, P. E. The Protein Data Bank. *Nucleic Acids Res.* **2000**, *28*, 235−242.

(2) Rose, P. W.; et al. The RCSB protein data bank: integrative view of protein, gene and 3D structural information. *Nucleic Acids Res.* **2017**, *45*, D271−D281.

(3) Rosenzweig, A. C. Metallochaperones: Bind and Deliver. *Chem. Biol.* **2002**, *9*, 673−677.

(4) Waldron, K. J.; Robinson, N. J. How do bacterial cells ensure that metalloproteins get the correct metal? *Nat. Rev. Microbiol.* **2009**, *7*, 25−35.

(5) Tus, A.; Rakipovic, A.; Peretin, G.; Tomic, S.; Sikic, M. BioMe: biologically relevant metals. *Nucleic Acids Res.* **2012**, *40*, W352−W357.

(6) Wang, L.; Yin, Y.-L.; Liu, X.-Z.; Shen, P.; Zheng, Y.-G.; Lan, X.-R.; Lu, C.-B.; Wang, J. Z. Current understanding of metal ions in the pathogenesis of Alzheimer's disease. *Transl. Neurodegener.* **2020**, *9*, 10.

(7) Knape, M. J.; Ballez, M.; Burghardt, N. C.; Zimmermann, B.; Bertinetti, D.; Kornev, A. P.; Herberg, F. W. Divalent metal ions control activity and inhibition of protein kinases. *Metallomics* **2017**, *9*, 1576−1584.

(8) Faller, P.; Hureau, C.; Berthoumieu, O. Role of Metal Ions in the Self-assembly of the Alzheimer's Amyloid-β Peptide. *Inorg. Chem.* **2013**, *52*, 12193−12206.

(9) Hoops, S. C.; Anderson, K. W.; Merz, K. M., Jr. Force field design for metalloproteins. *J. Am. Chem. Soc.* **1991**, *113*, 8262−8270.

(10) Babu, C. S.; Lim, C. Empirical Force Fields for Biologically Active Divalent Metal Cations in Water. *J. Phys. Chem. A* **2006**, *110*, 691−699.

(11) Joung, I. S.; Cheatham, T. E., III Determination of Alkali and Halide Monovalent Ion Parameters for Use in Explicitly Solvated Biomolecular Simulations. *J. Phys. Chem. B* **2008**, *112*, 9020−9041.

(12) Cheatham, M. B.; Yang, Y.; Wang, B.; Füsti-Molnár, L.; Weaver, M. N.; Merz, K. M., Jr. Structural Survey of Zinc-Containing Proteins and Development of the Zinc AMBER Force Field (ZAFF). *J. Chem. Theory Comput.* **2010**, *6*, 2935−2947.
(13) Pang, Y.-P. Successful molecular dynamics simulation of two zinc complexes bridged by a hydroxide in phosphotriesterase using the cationic dummy atom method. *Proteins: Struct., Funct., Bioinf.* **2001**, *45*, 183−189.
(14) Li, P.; Roberts, B. P.; Chakravorty, D. K.; Merz, K. M., Jr. Rational Design of Particle Mesh Ewald Compatible Lennard-Jones Parameters for +2 Metal Cations in Explicit Solvent. *J. Chem. Theory Comput.* **2013**, *9*, 2733−2748.
(15) Li, P.; Merz, K. M., Jr. Taking into Account the Ion-Induced Dipole Interaction in the Nonbonded Model of Ions. *J. Chem. Theory Comput.* **2014**, *10*, 289−297.
(16) Li, P.; Song, L. F.; Merz, K. M., Jr. Parameterization of Highly Charged Metal Ions Using the 12-6-4 LJ-Type Nonbonded Model in Explicit Water. *J. Phys. Chem. B* **2015**, *119*, 883−895.
(17) Jiang, Y.; Zhang, H.; Tan, T. Rational Design of Methodology-Independent Metal Parameters Using a Nonbonded Dummy Model. *J. Chem. Theory Comput.* **2016**, *12*, 3250−3260.
(18) Dang, L. X. Development of nonadditive intermolecular potentials using molecular dynamics: Solvation of Li^+ and F^- ions in polarizable water. *J. Chem. Phys.* **1992**, *96*, 6970.
(19) Grossfield, A.; Ren, P.; Ponder, J. W. Ion Solvation Thermodynamics from Simulation with a Polarizable Force Field. *J. Am. Chem. Soc.* **2003**, *125*, 15671−15682.
(20) Jiao, D.; King, C.; Grossfield, A.; Darden, T. A.; Ren, P. Simulation of Ca^{2+} and Mg^{2+} Solvation Using Polarizable Atomic Multipole Potential. *J. Phys. Chem. B* **2006**, *110*, 18553−18559.
(21) Piquemal, J.-P.; Perera, L.; Cisneros, G. A.; Ren, P.; Pedersen, L. G.; Darden, T. A. Towards accurate solvation dynamics of divalent cations in water using the polarizable amoeba force field: From energetics to structure. *J. Chem. Phys.* **2006**, *125*, 054511.
(22) Yu, H.; Whitfield, T. W.; Harder, E.; Lamoureux, G.; Vorobyov, I.; Anisimov, V. M.; MacKerell, A. D.; Roux, B. Simulating Monovalent and Divalent Ions in Aqueous Solution Using a Drude Polarizable Force Field. *J. Chem. Theory Comput.* **2010**, *6*, 774−786.
(23) Merz, K. M., Jr. Carbon dioxide binding to human carbonic anhydrase II. *J. Am. Chem. Soc.* **1991**, *113*, 406−411.
(24) Stote, R. H.; Karplus, M. Zinc binding in proteins and solution: a simple but accurate nonbonded representation. *Proteins* **1995**, *23*, 12−31.
(25) Darden, T.; York, D.; Pedersen, L. Particle mesh Ewald: An N·log(N) method for Ewald sums in large systems. *J. Chem. Phys.* **1993**, *98*, 10089.
(26) Essmann, U.; Perera, L.; Berkowitz, M. L.; Darden, T.; Lee, H.; Pedersen, L. G. A smooth particle mesh Ewald method. *J. Chem. Phys.* **1995**, *103*, 8577.
(27) Luty, B. A.; Tironi, I. G.; van Gunsteren, W. F. Lattice-sum methods for calculating electrostatic interactions in molecular simulations. *J. Chem. Phys.* **1995**, *103*, 3014.
(28) Kurtović, Z.; Marchi, M.; Chandler, D. Umbrella sampling molecular dynamics study of the dielectric constant of water. *Mol. Phys.* **1993**, *78*, 1155−1165.
(29) Wu, X.; Brooks, B. R. Isotropic periodic sum: A method for the calculation of long-range interactions. *J. Chem. Phys.* **2005**, *122*, 044107.
(30) Wu, X.; Brooks, B. R. The Homogeneity Condition: A Simple Way to Derive Isotropic Periodic Sum Potentials for Efficient Calculation of Long-Range Interactions in Molecular Simulation. *J. Chem. Phys.* **2019**, *150*, 214109.
(31) Wu, X.; Brooks, B. R. A double exponential potential for van der Waals interaction. *AIP Adv.* **2019**, *9*, 065304.
(32) Case, D. A. et al. *AMBER 19*; University of California: San Francisco, 2019.
(33) Case, D. A.; Cheatham, T. E., III; Darden, T.; Gohlke, H.; Luo, R.; Merz, K. M., Jr.; Onufriev, A.; Simmerling, C.; Wang, B.; Woods, R. J. The Amber biomolecular simulation programs. *J. Comput. Chem.* **2005**, *26*, 1668−1688.
(34) Mezei, M. The Finite Difference Thermodynamic Integration, Tested on Calculating the Hydration free Energy Difference between Acetone and Dimethylamine in Water. *J. Chem. Phys.* **1987**, *86*, 7084−7088.
(35) Mitchell, M. J.; McCammon, J. A. Free Energy Difference Calculations by Thermodynamic Integration: Difficulties in Obtaining a Precise Value. *J. Comput. Chem.* **1991**, *12*, 271−275.
(36) Kollman, P. Free Energy Calculations: Applications to Chemical and Biochemical Phenomena. *Chem. Rev.* **1993**, *93*, 2395−2417.
(37) Simonson, T.; Carlsson, J.; Case, D. A. Proton Binding to Proteins: pKa Calculations with Explicit and Implicit Solvent Models. *J. Am. Chem. Soc.* **2004**, *126*, 4167−4180.
(38) Gauss, C. F. *Methodus nova integralium valores per approximationem inveniendi*; Goettingen, 1886; Vol. 3, pp 163−196.
(39) Pearlman, D. A.; Charifson, P. S. Are Free Energy Calculations Useful in Practice? A Comparison with Rapid Scoring Functions for the p38 MAP Kinase Protein System. *J. Med. Chem.* **2001**, *44*, 3417−3423.
(40) Michel, J.; Verdonk, M. L.; Essex, J. W. Protein-Ligand Binding Affinity Predictions by Implicit Solvent Simulations: A Tool for Lead Optimization? *J. Med. Chem.* **2006**, *49*, 7427−7439.
(41) Shannon, R. D. Revised effective ionic radii and systematic studies of interatomic distances in halides and chalcogenides. *Acta Crystallogr.* **1976**, *32*, 751.
(42) Wang, J.; Hou, T. Application of Molecular Dynamics Simulations in Molecular Property Prediction II: Diffusion Coefficient. *J. Comput. Chem.* **2011**, *32*, 3505−3519.
(43) Skinner, L. B.; Huang, C.; Schlesinger, D.; Pettersson, L. G. M.; Nilsson, A.; Benmore, C. J. Benchmark oxygen-oxygen pair-distribution function of ambient water from x-ray diffraction measurements with a wide Q-range. *J. Chem. Phys.* **2013**, *138*, 074506.
(44) Lide, D. R. *CRC Handbook of Chemistry and Physics*, 85th ed.; CRC Press, 2004.
(45) Jorgensen, W. L.; Chandrasekhar, J.; Madura, J. D.; Impey, R. W.; Klein, M. L. Comparison of simple potential functions for simulating liquid water. *J. Chem. Phys.* **1983**, *79*, 926−935.
(46) Holz, M.; Heil, S. R.; Sacco, A. Temperature-dependent self-diffusion coefficients of water and six selected molecular liquids for calibration in accurate 1H NMRPFG measurements. *Phys. Chem. Chem. Phys.* **2000**, *2*, 4740−4742.
(47) *MATLAB*, R2015b; The MathWorks Inc.: Natick, Massachusetts, 2018.
(48) Marcus, Y. Thermodynamics of solvation of ions. Part 5. −Gibbs free energy of hydration at 298.15 K. *J. Chem. Soc., Faraday Trans.* **1991**, *87*, 2995−2999.
(49) Marcus, Y. Ionic radii in aqueous solutions. *Chem. Rev.* **1988**, *88*, 1475−1498.
(50) Takafumi, M.; Iwao, W.; Shigero, I. Amplitude in EXAFS and Ligand Exchange Reaction of Hydrated 3d Transition Metal Complexes. *Chem. Lett.* **1988**, *17*, 1073−1076.
(51) Ohtaki, H.; Radnai, T. Structure and dynamics of hydrated ions. *Chem. Rev.* **1993**, *93*, 1157−1204.
(52) Jalilehvand, F.; Spångberg, D.; Lindqvist-Reis, P.; Hermansson, K.; Persson, I.; Sandström, M. Hydration of the Calcium Ion. An EXAFS, Large-Angle X-ray Scattering, and Molecular Dynamics Simulation Study. *J. Am. Chem. Soc.* **2001**, *123*, 431−441.
(53) Smirnov, P. R.; Trostin, V. N. Structural parameters of close surroundings of Sr2+ and Ba2+ ions in aqueous solutions of their salts. *Russ. J. Gen. Chem.* **2011**, *81*, 282−289.
(54) Mamatkulov, S.; Schwierz, N. Force fields for monovalent and divalent metal cations in TIP3P water based on thermodynamic and kinetic properties. *J. Chem. Phys.* **2018**, *148*, 074504.
(55) Vanýsek, P. Ionic conductivity and diffusion at infinite dilution *Handbook of Chemistry and Physics*, 1992/93 ed.; CRC Press: Boca Raton, 1992; pp 5-111−5-113.

https://dx.doi.org/10.1021/acs.jctc.0c01267
J. Chem. Theory Comput. 2021, 17, 1086−1097

(56) Huang, J.; Lemkul, J. A.; Eastman, P. K.; MacKerell, A. D., Jr Molecular Dynamics Simulations Using the Drude Polarizable Force Field on GPUs with OpenMM: Implementation, Validation, and Benchmarks. *J. Comput. Chem.* **2018**, *39*, 1682−1689.
(57) Leonard, A. N.; Simmonett, A. C.; Pickard, F. C.; Huang, J.; Venable, R. M.; Klauda, J. B.; Brooks, B. R.; Pastor, R. W. Comparison of Additive and Polarizable Models with Explicit Treatment of Long-Range Lennard-Jones Interactions Using Alkane Simulations. *J. Chem. Theory Comput.* **2018**, *14*, 948−958.
(58) Yu, Y.; Krämer, A.; Klauda, J. B.; Pastor, R. W. Modifying the CHARMM36 Lipid Force Field for LJ-PME Simulations. *Biophys. J.* **2020**, *118*, 87a.
(59) Wennberg, C. L.; Murtola, T.; Páll, S.; Abraham, M. J.; Hess, B.; Lindahl, E. Direct-Space Corrections Enable Fast and Accurate Lorentz-Berthelot Combination Rule Lennard-Jones Lattice Summation. *J. Chem. Theory Comput.* **2015**, *11*, 5737−5746.
(60) Hess, B.; Kutzner, C.; van der Spoel, D.; Lindahl, E. Gromacs 4: Algorithms for highly efficient, load-balanced, and scalable molecular simulation. *J. Chem. Theory Comput.* **2008**, *4*, 435−447.

https://dx.doi.org/10.1021/acs.jctc.0c01267
J. Chem. Theory Comput. 2021, 17, 1086−1097